Biosensors and Bioelectronics 198 (2022) 113821

Contents lists available at ScienceDirect

Biosensors and Bioelectronics

journal homepage: www.elsevier.com/locate/bios

Dispersion-to-localization of catalytic hairpin assembly for sensitive sensing and imaging microRNAs in living cells from whole blood

Huijie Bai [a], Yurong Yan [a,1], Dandan Li [b], Ningke Fan [a], Wenqian Cheng [a], Wei Yang [a], Huangxian Ju [c], Xinmin Li [a,d,**], Shijia Ding [a,*]

[a] Key Laboratory of Clinical Laboratory Diagnostics (Ministry of Education), College of Laboratory Medicine, Chongqing Medical University, Chongqing, 400016, China
[b] Department of Laboratory Medicine, The Second Affiliated Hospital of Chongqing Medical University, Chongqing, 400010, China
[c] State Key Laboratory of Analytical Chemistry for Life Science, Department of Chemistry, Nanjing University, Nanjing, 210023, China
[d] Department of Laboratory Medicine, Chongqing Hospital of Traditional Chinese Medicine, Chongqing, 400016, China

ARTICLE INFO

Keywords:
Dispersion-to-localization
Catalytic hairpin assembly
MicroRNAs
Living cells imaging
Whole blood

ABSTRACT

Localized DNA circuits have shown good performance regarding reaction rate and sensitivity for sensing intracellular microRNAs (miRNAs). However, these methods reported recently require large kinds of DNA strands and suffer from low signal-to-background (S/B) ratio, which hinder their clinical application. To circumvent these issues, we herein developed a novel strategy for sensitive sensing and imaging miRNAs in living cells based on dispersion-to-localization of catalytic hairpin assembly (DL-CHA). This strategy consists of only three classes of DNA strands (two hairpins and a linker strand), which largely reduces sequence design complexity. Additionally, owing to the unique engineering of the substrate transformation from dispersion to localization, the DL-CHA exhibits not only minimal background leakage but also intensive signal amplification, thus significantly improving the S/B ratio. In particular, the simple sensing method is capable of imaging miRNAs in cells from clinical blood samples for the diagnosis of breast cancer. Therefore, this work provides a powerful tool for intracellular molecules detection and gives a much broader design space for constructing high-performance DNA circuits.

1. Introduction

MicroRNAs (miRNAs) are small (about 22 nucleotides) endogenous non-coding RNAs, which exactly regulate gene expression by binding to specific mRNA targets and facilitating their degradation or translational inhibition (Gebert and MacRae, 2019; Tricoli and Jacobson, 2007). This regulatory mechanism enables miRNAs to play vital roles in various cellular activities (Mendell and Olson, 2012). Also, the abnormal expression of miRNAs is closely correlated with the initiation, progression, and drug resistance of diseases, highlighting that miRNAs have great potential as critical biomarkers for early diagnosis and prognosis of diseases (Anfossi et al., 2018; Goodall and Wickramasinghe, 2021). Thus, efficient and reliable detection of miRNAs is highly desirable, particularly in situ analysis of living cells. However, it remains a challenge for accurate sensing of intracellular miRNAs owing to their low abundance, high sequence homology, and heterogeneous expression in different times and locations (Deng et al., 2017; Meng et al., 2021).

At present, considerable efforts have been made towards the development of strategies to sense and image intracellular miRNAs (Peng et al., 2020; Qing et al., 2019). These methods included molecular beacon-based nanoflares (Choi et al., 2015; Gao et al., 2020), enzyme-amplified technologies (rolling circle amplification and polymerase-powered strand displacement) (Deng et al., 2014; Xue et al., 2018; Yang et al., 2018), nanomaterial-assisted strategies (Zhu et al., 2019) and nonenzymatic DNA circuits (DNAzyme (Duan et al., 2021; Wei et al., 2020), catalytic hairpin assembly (CHA) (Karunanayake Mudiyanselage et al., 2018; Li et al., 2020a; Liu et al., 2020b), hybridization chain reaction (HCR) (Cheglakov et al., 2015; Wei et al., 2018a), and entropy-driven circuit (EDC) (Liang et al., 2017; Zhang et al., 2019). Despite remarkable successes, these protocols cover at least one of the

* Corresponding author.
** Corresponding author. Key Laboratory of Clinical Laboratory Diagnostics (Ministry of Education), College of Laboratory Medicine, Chongqing Medical University, Chongqing, 400016, China.
E-mail addresses: xinmnli@163.com (X. Li), dingshijia@163.com (S. Ding).
[1] These authors contribute equally to this work.

https://doi.org/10.1016/j.bios.2021.113821
Received 12 August 2021; Received in revised form 4 November 2021; Accepted 17 November 2021
Available online 23 November 2021

following drawbacks: deficient sensitivity as a result of the equivalent reaction ratio of target and signal (Huo et al., 2019; Li et al., 2020b), requirement for bulky exogenous enzymes that may change the expression of intracellular miRNA (Liu et al., 2020b), slow reaction kinetics because of the random collision of free diffusible reactants (Chatterjee et al., 2017; Liu et al., 2020a; Teichmann et al., 2014), and cumbersome preparation process of nanomaterials (Liu et al., 2016).

Nonenzymatic localized DNA circuits that reactants are placed into proximity in a confined space offer a potential tool to address the issues. The spatial localization of reactants endows these circuits with faster reaction kinetic and higher sensitivity, which are deemed as valuable strategies in biosensing and bioimaging field (Ren et al., 2018). Recent work has achieved in situ analysis of miRNA using the localization of hairpin reactants on DNA nanomaterials such as nanowire (Wei et al., 2018b; Wu et al., 2020; Zhu et al., 2020), quadrangular (Lin et al., 2021), tetrahedron (Xing et al., 2021), and cube (Liu et al., 2019). Nevertheless, these localized DNA circuits have certain limitations that need to be addressed through novel design approaches. First, the prefabrication of localized substrates requires numerous kinds of DNA strands, which increases the sequence design complexity. Second, the leakage reaction is severe, because diverse DNA hairpins simultaneously assembled into a compact space are more prone to interact non-specifically, leading to the low signal-to- background (S/B) ratio (Liu et al., 2020a; Sun et al., 2018). This provides motivation for the design of a localized DNA circuit with few strands and high S/B ratio.

Herein, we designed a novel sensing paradigm, DNA ladder formed by dispersion-to-localization of catalytic hairpin assembly (DL-CHA), for sensitive miRNAs detection and imaging in living cells (Scheme 1). Compared with other strategies, our sensing system contains only two classes of hairpins and a linker strand to reduce strand complexity. Five hairpins H1 and H2 are separately bound to linker strand L, forming localized LH1 and LH2 to prevent nonspecific reaction caused by the colocalization of diverse hairpins. Self-quenched H1 is labeled with 5-Carboxyfluorescein (FAM) and Black Hole Quenchers1 (BHQ1) at appropriate position while H2 without any modification. Under the response of intracellular miR-21, H1 is opened and a toehold initially locked in the H1 stem becomes available to initiate the unwinding of H2 and displacement of the target (dispersive CHA), inducing the colocalization of LH1 and LH2. Then, the displaced target moves forward quickly powered by strand displacement reaction in the combined space (localized CHA), resulting in the hybridization of the LH1 and LH2 each other, the formation of DNA ladder, and the production of significant fluorescence signal for intracellular miRNA sensing. Integrated the advantages of few kinds of strands, minimal leakage, and rapid reaction rate, the developed DL-CHA is expected to be a promising tool for biomolecules imaging in the field of early diagnostics.

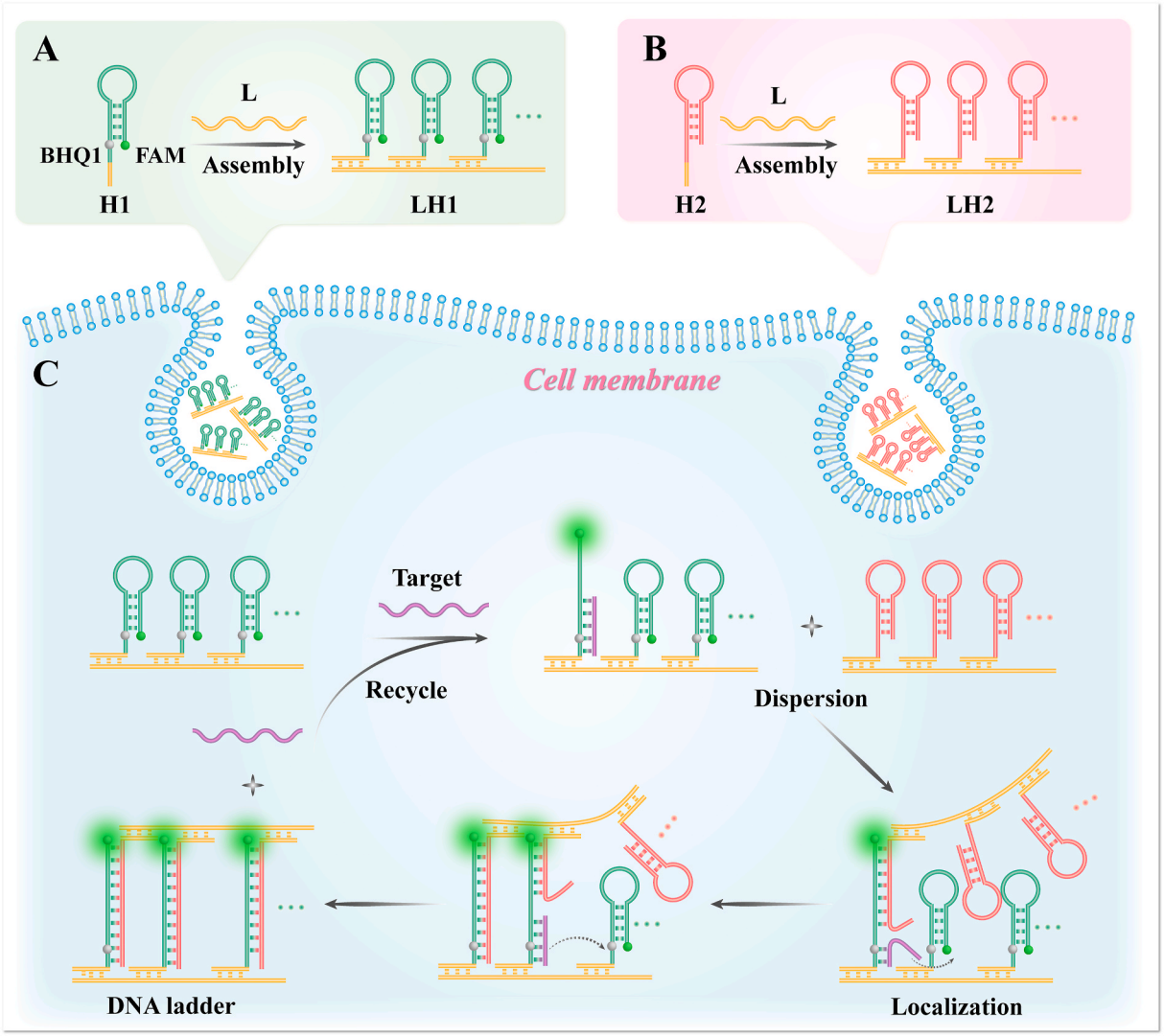

Scheme 1. Schematic illustration of intracellular formation of DNA ladder via DL-CHA for visualization of miRNA in living cells. (A and B) The prefabrication of localized LH1 and LH2. (C) The operation of DL-CHA responding to intracellular miR-21.

2. Experimental section

2.1. Materials and reagents

The oligonucleotides (Table S1) and red cell lysis buffer were purchased from Sangon Biotech (Shanghai, China). All synthetic oligonucleotides were dissolved in tris-ethylenediaminetetraacetic acid buffer (pH 8.0) and stored at −20 °C. 20 bp DNA Ladder was bought from TaKaRa Biotech (Dalian, China). Gold View was purchased from SBS Genetech (Beijing, China). All cell lines including normal epithelial breast cell line (MCF-10A), breast cancer cell lines (MCF-7 and SK-BR3), and liver cancer cell line (HepG2) were obtained from American Type Culture Collection (ATCC, USA). Fetal bovine serum (FBS), Dulbecco's modified Eagle's medium (DMEM), and penicillin-streptomycin were purchased from Hyclone (USA). All reagents were analytical grade.

2.2. Apparatus

The fluorescence spectra were measured on a Cary Eclipse Fluorescence Spectrophotometer (Agilent Technologies, CA). The gel electrophoresis was carried out on the electrophoresis instruments (Bio-Rad, USA), and the ChemiDoc XRS system (Bio-Rad, USA) was used for the gel image. The size and morphology of ZNS was characterized by atomic force microscope (AFM) dimension icon (BrukerAXS, Germany). The fluorescence intensity of cells was measured on a CytoFLEX Flow Cytometer (Beckman Coulter, USA). Confocal fluorescence imaging of cells was performed on a TCSSP8 confocal laser scanning microscope (Leica, Germany).

2.3. Preparation of localized substrates (LH1 and LH2)

Before use, H1 and H2 were annealed respectively in the hybridization buffer (20 mM Tris, 140 mM NaCl and 5 mM KCl, pH 7.5) at 95 °C for 5 min and slowly cooled to room temperature over 2 h. Then, 10 μL of the annealed H1 and H2 (20 μM) were separately incubated with 2 μL of L strand (20 μM) at 37 °C for 35 min to assemble LH1 and LH2.

2.4. Electrophoresis analysis

2% Agarose gel electrophoresis was performed using 1 × TBE buffer, and the loaded samples contained 10 μL of reaction sample and 2 μL of 6 × loading buffer. The gel electrophoresis was run at 110 V for 30 min and imaged via the ChemiDoc XRS system.

2.5. In vitro detection of miR-21

To perform the DL-CHA reaction in vitro, equal volumes of LH1 and LH2 (25 μL) were mixed with varying concentrations of target miRNA in the hybridization buffer to give a total volume of 100 μL, and the final concentrations of LH1 and LH2 were 250 nM. After the mixture was incubated at 37 °C for 30 min, the produced fluorescence signal was measured between 500 and 600 nm with the excitation wavelength of 488 nm. For real-time fluorescence experiment, 100 μL of the mixture containing 25 nM miR-21, 250 nM H1, and 250 nM H2 was added in cuvette immediately for fluorescence recording. Fluorescence spectra were recorded with excitation at 488 nm and emission at 520 nm. The slit width was set to be 5 nm for both excitation and emission. The collection time interval was set to 0.1 min.

2.6. Serum stability assay of DNA substrates

LH1 and H1 were spiked with FBS respectively to a final concentration of 250 nM in 10% FBS. The two solutions were incubated at 37 °C for 8 h, and the degradation of LH1 and H1 was evaluated by recording fluorescence signal and performing 2% agarose gel electrophoresis every 2 h.

2.7. Cell culture and cytotoxicity assay

In addition to the special culture medium for MCF-10A, the others were cultured in DMEM containing 10% FBS and supplemented with 100 μg/mL streptomycin and 100 U/mL penicillin at 37 °C in a humidified incubator containing 5% CO_2. For cytotoxicity assay, 1×10^6 MCF-7 cells were seeded in 96-well plates in a total volume of 100 μL/well. After incubation for 24 h, the medium was removed, and serial concentrations of the probes were added for 4 h incubation. Cells incubated with only the medium served as control. Then, 10 μL of Cell Counting Kit-8 (CCK-8) solution and 90 μL of serum-free medium were added to each well with incubation at 37 °C for 4 h. Then, the cell viability was determined by measuring the absorbance at 490 nm by a multi-detection microplate reader.

2.8. Confocal fluorescence imaging and flow cytometry assay

Cells of interest were seeded on cell slides in 24-well microplate for 24 h at 37 °C, then incubated with 200 μL of culture medium containing 250 nM LH1 and LH2 for 4 h at 37 °C. After washing twice with phosphate buffer saline (PBS), Hoechst 33,342 was added for cell nucleus staining. Then, the fluorescence of the cells was visualized by TCSSP8 confocal scanning system from 510 to 550 nm with the excitation wavelength of 488 nm for FAM. For flow cytometric analysis, the suspended cell solution was centrifuged at 2000 rpm for 5 min and washed with PBS three times. Afterwards, the cells were resuspended in PBS for flow cytometric analysis.

2.9. Clinical sample analysis

Whole blood samples of breast cancer patients or healthy individuals were gained from The Second Affiliated Hospital of Chongqing Medical University with ethical approval. Referring to the manufacturer's instructions, the samples were firstly treated with 6 times the volume of red cell lysis buffer and mixed sufficiently for 5 min. Next, the mixture was centrifuged at 4000 rpm for 3 min. Then, the supernatant was gently discarded to remove lysate and other impurities, and resuspended by PBS. The process was repeat twice until the supernatant was clear and precipitate was faint pink. After that, the collected cells were incubated with 250 nM LH1 and LH2 for 4 h at 37 °C and further stained with Hoechst for 5 min. Ultimately, the fluorescence of the cells was visualized by TCSSP8 confocal scanning system from 510 to 550 nm with the excitation wavelength of 488 nm for FAM.

3. Results and discussion

3.1. Characterization of DL-CHA

The substrate preassembly of DL-CHA was first verified by recording the change of fluorescence signal with the hybridization of L strand labeled with BHQ1 at different sites and H1 tagged with FAM. As shown in Fig. 1A, the signal significantly decreased with the extension of hybridization time and reached to the lowest value at 35 min, indicating the full binding of L and H1. Compared to the localized DNA circuits reported recently that needed several hours and multiple link steps to assemble substrates (Ren et al., 2018; Wei et al., 2018b; Zhu et al., 2020), DL-CHA achieved substrate assembly in a single step with tens of minutes. Then, agarose gel electrophoresis was used to characterize the reaction process of DL-CHA. As shown in Fig. 1B, lanes from 1 to 4 were miR-21, L, H1, and H2, respectively. After hybridization of L and H1 or H2, the original bands disappeared and new bands with lower mobility were observed (lane 5 and 6), further indicating the successful formation of LH1 and LH2. When mixing LH1 and LH2, no extra bands emerged, suggesting that weak leakage reaction happened in the dispersion of LH1 and LH2 (lane 7). By contrast, new bands with a much slower gel mobility appeared after adding target miR-21 to the mixture, confirming

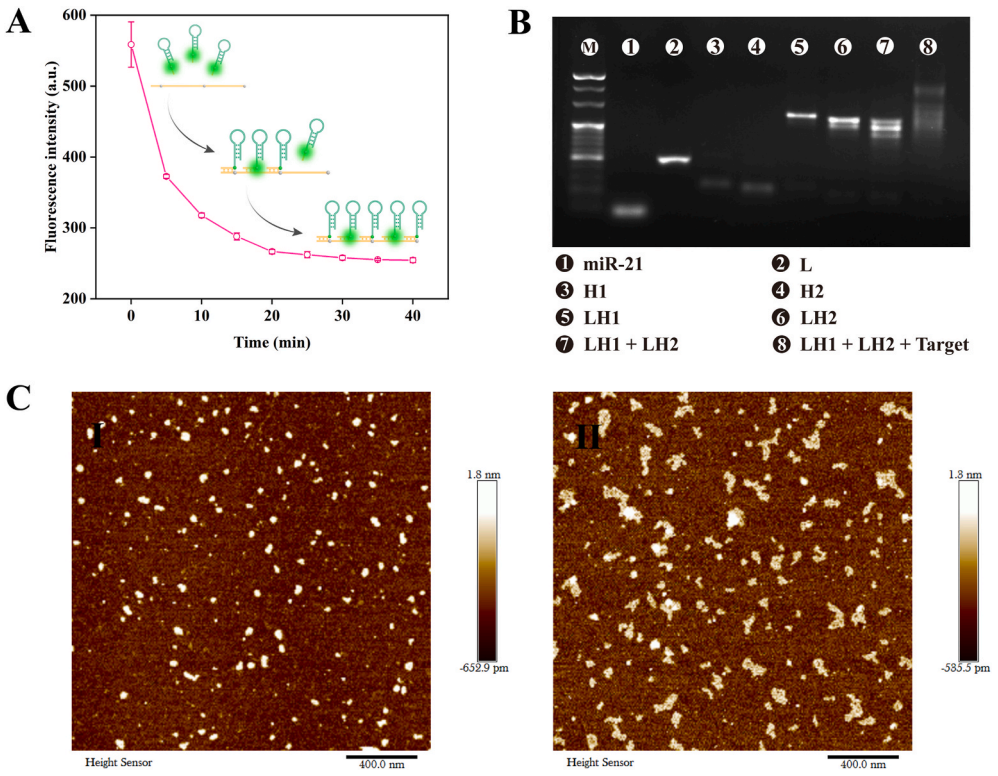

Fig. 1. Characterization of DL-CHA. (A) Evaluation of the assembly of L and H1 by monitoring the change of fluorescence signal with the increase of hybridization time at 37 °C. The concentration of H1 is 250 nM. (B) Agarose gel electrophoresis (2%) characterization of the reaction process of DL-CHA. The concentrations of DNA substrates are constant (1 μM). (C) AFM images of different samples: (I) LH1 + LH2 and (II) DNA ladder formed by DL-CHA. Scale bar is 400 nm.

that the localization of LH1 and LH2 formed the DNA architecture with higher molecular weight (lane 8). Furthermore, the architecture was characterized by AFM, and the results were showed in Fig. 1C. Compared to the dispersed LH1 and LH2 (I), larger size complex could be noticed as the conformation of DNA ladder (II). These results verified that the substrates realized the transformation from dispersion to localization under the response of miR-21 and DL-CHA was successfully constructed.

3.2. Thermodynamics and kinetic analysis for DL-CHA

To evaluate the operation of DL-CHA, the corresponding thermodynamics and kinetic parameters were analyzed. The entire process was conducted in an isothermal and isobaric environment, which was expressed in Fig. 2A. According to the van't Hoff equation, the Gibbs free energy change is given by

$$\Delta G = \Delta G_{\text{DNA ladder}} - \Delta G_{LH1} - \Delta G_{LH2} + RT \ln Q \quad (1)$$

where R is the gas constant (8.314 J/mol•K), T is the temperature in kelvin unit (K), and Q is the reaction quotient. $\Delta G_{\text{DNA ladder}}$, ΔG_{LH1}, and ΔG_{LH2} are the standard free energies, which can be worked out using NUPACK software as below. The software parameter settings were depicted in supplementary material.

$$\Delta G - RT \ln Q = \Delta G_{\text{DNA ladder}} - \Delta G_{LH1} - \Delta G_{LH2} = -73.65 \text{ kcal/mol} \quad (2)$$

When the reaction is at equilibrium, $\Delta G = 0$, Giving

$$RT \ln Q = 73.65 \text{ kcal/mol} \quad (3)$$

According to equation (3), we can calculate $Q = 8.31 \times 10^{51}$. Also, Q can be expressed as below.

$$Q = \frac{[\text{DNA ladder}]}{[LH1][LH2]} \quad (4)$$

Herein, the initial concentrations of LH1 and LH2 are 250 nM, and supposing that the final concentration of DNA ladder is X nM. Then, the following equation is gained based on equation (4):

$$\left(10^{-9}X\right) \Big/ \left[\left(10^{-9}(250 - X)\right]^2 = 8.31 \times 10^{51}\right.$$

Therefore, X is estimated to be between 249.9999 and 250 nM using the bisection method, suggesting a potential systemic fractional conversion of more than 99.99% without regard to the reaction time.

To prove the enhanced reaction kinetics of DL-CHA, several physicochemical parameters were first evaluated based on the collision theory ($V = 1/CN$) in which V is local sphere volume, C is the concentration of reactants, and N is the Avogadro constant. If the solution only contains 250 nM H1, the volume of the sphere would be $V = 6.64 \times 10^{-18}$ L, and the radius of this sphere would be $r = (3V/4\pi)^{1/3} = (3/CN4\pi)^{1/3} =$ 117 nm. In view of the hybridization of L strand with multiple H1, the distance between H1 is reduced to about 5.1 nm (15 bp). Hence, the local concentration of H1 in LH1 is calculated to 2.99 mM, which is 12,000-fold higher than that of free H1 (the upper part of Fig. 2B). Similarly, supposing that the solution contains 250 nM LH1 and LH2, the distance between LH1 and LH2 is cut down from 117 to 15.64 nm (46 bp length of H1–H2 duplex) once the dispersive LH1 and LH2 are converted into colocalization (the lower part of Fig. 2B). As a result, the local concentrations of the linked LH1-LH2 in DL-CHA are calculated to 100 μM, which is 400-fold as high as that of the free reactants. Owing to the direct proportion of the collision frequency to the concentrations of reactants, the increased local concentration could enhance the reaction rate of DL-CHA in theory.

Furthermore, real-time fluorescence experiments of DL-CHA and conventional CHA were carried out to verify the theoretical analysis. The fluorescence intensity was recorded within 60 min in response to 25 nM miR-21. As depicted in Fig. 2C, the faint fluorescence signal was detected from both systems in the absence of miR-21. In the presence of miR-21, the fluorescence intensity of DL-CHA increased rapidly and was

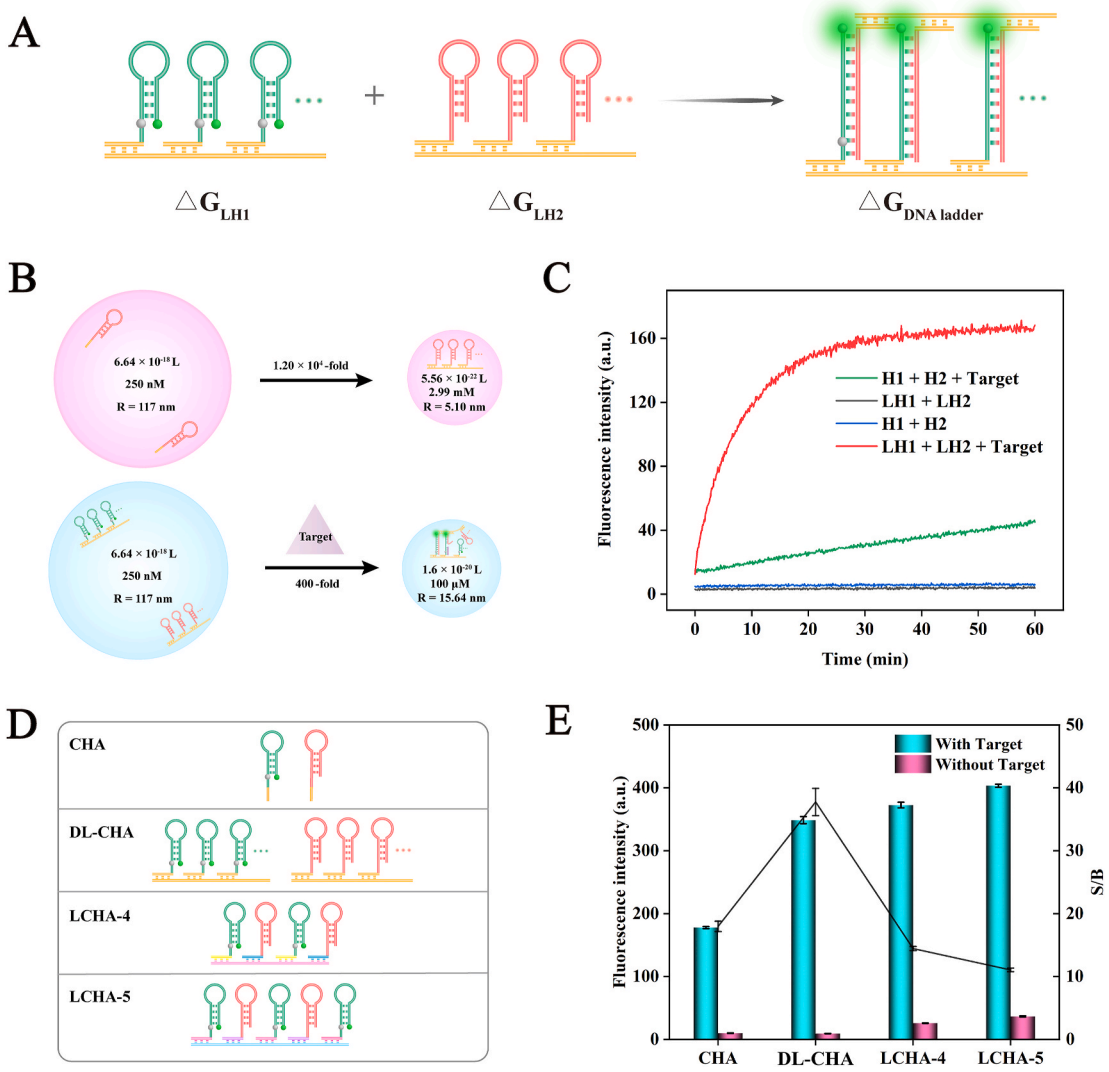

Fig. 2. (A) Reaction equation of DL-CHA with thermodynamic parameters. (B) Comparison of the reaction area and local concentration of H1 and LH1 (the upper part) and LH1 and LH2 for DL-CHA (the lower part). (C) Time-dependent fluorescence spectra of DL-CHA and CHA containing 250 nM H1 and H2 in response to 25 nM miR-21. (D) Schematic illustration of the reaction substrates of CHA, DL-CHA, and LCHA. (E) Comparison of the S/B ratio of CHA, DL-CHA, and LCHA containing 250 nM H1 and H2 in response to 250 nM miR-21 upon 30 min reaction time. The data error bars indicate mean ± SD (n = 3).

closed to summit at around 30 min, while CHA produced a much slower fluorescence enhancement and the highest signal still not be gained at 60 min. The theoretical and experiment results got the coincident conclusion that DL-CHA possessed fast reaction rate.

3.3. High S/B ratio of DL-CHA

The S/B ratio of DL-CHA was investigated and compared with that of conventional LCHA and CHA. LCHA contained a long DNA strand hybridized with H1 and H2 simultaneously (Fig. 2D). As shown in Fig. 2E, the signal leakage of DL-CHA was slightly below that of CHA, which was consistent with the results of real-time fluorescence experiments (Fig. 2C). This might be because the improved size and molecular weight of LH1 and LH2 relative to free hairpins (H1 and H2) mitigated their Brownian movement, resulting in the reduction of nonspecific reaction in the dispersive CHA. Although the signal of LCHA responded to 250 nM target miR-21 just higher than that of DL-CHA upon 30 min reaction time, the leakage reaction of LCHA increased with the increase of the number of hairpins, which was severer than that of DL-CHA. This was ascribed to the fact that different hairpins (H1 and H2) of LCHA tended to happen more nonspecific reaction. In general, the S/B ratio of DL-CHA reached to about 37.8, which were 2.6–3.4 times to those of CHA and LCHA. In addition, the versatility of DL-CHA in the reduction of background signal was investigated by detecting miR-155. As expected, the DL-CHA also exhibited higher signal output with almost half of leakage than that of CHA (Fig. S1). These results demonstrated the considerable advantages of DL-CHA in minimal leakage reaction and high signal gain due to the conversion from dispersion to localization.

3.4. Sensing miR-21 in vitro

Given the noteworthy advantages of DL-CHA, analytic capability of this sensing strategy was further evaluated in vitro. To demonstrate the high sensitivity of DL-CHA, the fluorescence signals of DL-CHA (Fig. 3A), CHA (Fig. 3D), and H1 (Fig. 3G) in response to target miRNA were respectively monitored and compared. The signals of DL-CHA (Fig. 3B) enhanced rapidly with the increase of miR-21 concentration compared to those of CHA (Fig. 3E) and H1 (Fig. 3H). DL-CHA responded to miR-21 in a broad linear range from 100 pM to 100 nM with the lowest detectable concentration (LDC) of 100 pM (Fig. 3C), which was comparable to and even lower than those of the localized DNA circuits reported recently (Li et al., 2021; Liu et al., 2019; Yang et al., 2019; Zhu

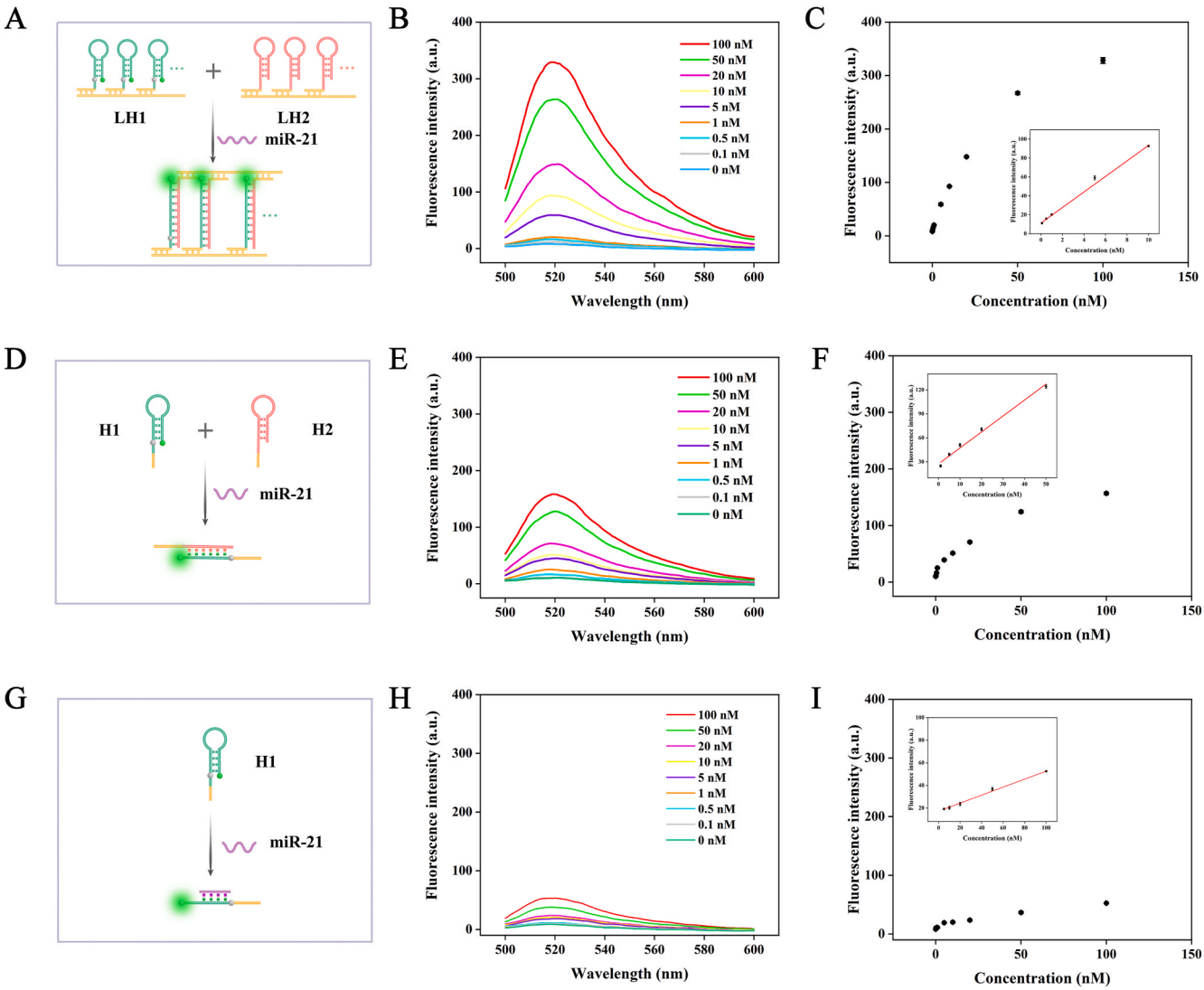

Fig. 3. Evaluation of the sensitivity of DL-CHA, CHA, and H1. Schematic and fluorescence spectra of (A, B) DL-CHA, (D, E) CHA, and (G, H) H1 responding to miR-21 at different concentrations and their corresponding calibration curves (C, F, and I). The data error bars indicate mean ± SD (n = 3).

et al., 2020). The linear ranges were 1–50 nM for CHA with LDC of 1 nM (Figure 3F) and 5–100 nM for H1 with LDC at 5 nM (Fig. 3I), respectively. By contrast, the LDC for DL-CHA was about 10-fold lower than that of CHA and 50-fold lower than that of H1. These results demonstrated the enhanced sensitivity of DL-CHA.

Aside from high sensitivity, good specificity is another crucial parameter for miRNAs sensing owing to their high sequence similarity. To evaluate the specificity of DL-CHA toward miR-21, contrastive substances including a series of targets with various base mutation and family members of miRNAs were analyzed by DL-CHA. As shown in Fig. S2, only miR-21 triggered significantly enhanced fluorescence signal. In contrast, all other miRNAs exhibited ignorable fluorescence intensities. The signals of miR-21 in DL-CHA were 27.7–39.1 times to those of contrastive substances at the same concentration. These results demonstrated the excellent specificity of DL-CHA to recognize target miRNA among family members.

Before the application of DL-CHA in the intracellular fluid, the structural stability of LH1 needs to be evaluated to determine that fluorescence signal is from DNA ladder rather than fluorescent dyes released by nuclease degradation. Thus, the LH1 incubated in 10% FBS for different lengths of time was analyzed by fluorescence and gel electrophoresis, respectively. As depicted in Fig. S3A, free self-quenched H1 in 10% FBS showed gradually enhanced fluorescence signals with the increase of incubation time. In contrast, the fluorescence signals of LH1 had minimal change, even long-term incubation (over 6 h) in 10% FBS. Furthermore, the electrophoretic analysis also showed that LH1 could sustain their structure at least 6 h, which was much less degradation than free H1 (Fig. S3B). This might be because the localized DNA structure of LH1 produced the steric hindrance stopping nuclease from accessing H1.

3.5. *Intracellular imaging of miRNAs via DL-CHA*

Benefiting from the superior performance of DL-CHA in vitro, the function of this strategy in living cells was further studied. First, the cytotoxicity of the localized substrates was evaluated through a standard colorimetric CCK-8 assay on MCF-7 cells. As shown in Fig. S4, after MCF-7 cells were treated with different concentrations of LH1 and LH2 from 10 to 500 nM for 4 h, the cells remained 86% viability even at the highest substrate concentration. These results demonstrated the good biocompatibility of DL-CHA. Then, the optimal incubation time between cells and the localized substrates was investigated by monitoring fluorescence intensity of DL-CHA in response to intracellular miR-21, and the results showed that the brightest fluorescence could be obtained at 4 h (Fig. S5). The long incubation time was attributed to the transfection process.

To demonstrate the signal amplification ability of DL-CHA for intracellular miR-21 sensing, MCF-7 cells were treated with different DNA reaction substrates, and the results were depicted in Fig. 4A. Compared to these control groups (MCF-7 cells with CHA and H1), MCF-7 cells with DL-CHA revealed bright green fluorescence owing to the robust signal amplification of target-induced localized DNA circuits. As shown in Fig. 4B, the fluorescence intensity from DL-CHA was 10.9 times than that of imaging with H1 and 2.48 times than that of imaging with CHA amplification. The difference was statistically significant ($P < 0.001$). Flow cytometry analysis was also used to record the fluorescence intensity of MCF-7 cells incubated with DL-CHA and CHA (Fig. S6), and the results were in accordance with confocal fluorescence images. These results demonstrated that the high signal amplification ability of DL-CHA for intracellular miR-21 imaging.

Owing to the vary of miRNA expression levels in same cancer cells with tumor progression, the ability of the DL-CHA to sense the changes of intracellular miR-21 needs to be confirmed. To perform this study, MCF-7 cells were divided into three groups in parallel: group I was transfected with the miR-21 mimics that could improve miR-21 expression, group II was an untreated group as a control, and group III was transfected with anti-miR-21 sequence that was applied to inhibit miR-21 expression. As shown in Fig. 5A, compared to group III that displayed negligible fluorescence signal, group I yielded obvious fluorescence signal, and the fluorescence signal of group II was situated between the previous two groups. The corresponding fluorescence intensity was evaluated in Fig. 5B. These results demonstrated that DL-CHA was capable of perceiving fluctuations of miRNA level in living cells.

Considering that the expression levels of miRNA in diverse cell lines are different, it is essential to evaluate whether the DL-CHA sensing system could be used to image miR-21 in other cells. Apart from MCF-7 cells, different cancerous cell lines (SK-BR3 and HepG2) and normal MCF-10A cells were employed. As shown in Fig. 5C, obvious green fluorescence appeared in SK-BR3 and HepG2 cells, while there was almost no fluorescence in MCF-10A cells. The mean fluorescence intensity of the MCF-10A was 316.5 and 315.0 times lower than that of SK-BR3 and HepG2 respectively as shown in Fig. 5D, the difference was statistically significant ($P < 0.001$). These results indicated the robust ability of DL-CHA to sense target miRNA in different kinds of tumor cells.

The few kinds of DNA strands and simple sequence design of DL-CHA motivated us to further evaluate its versatility. Thus, sensing and imaging of multiple miRNAs (miR-21 and miR-155) simultaneously in single living cell was implemented by simple changing target-specific sequence. As shown in Fig. S7, MCF-7 cells revealed high fluorescence signals of FAM for miR-21 and Cy5 for miR-155, because miR-155 was also over-expression in the cells, while very little fluorescence was observed in MCF-10A cells. These results demonstrated the high versatility of DL-CHA.

3.6. Clinical application of DL-CHA

Encouraged by the excellent performance of DL-CHA in living cells, its application in clinical samples was studied. These samples were obtained from three healthy individuals and three breast cancer patients. As shown in Fig. S8A, the collected cells (I-III) from healthy individuals generated hardly fluorescence, while obviously enhanced fluorescence signals were observed in these cells (Ⅳ-Ⅵ) acquired from patients with breast cancer. By comparison to fluorescence intensity in different samples using our developed DL-CHA strategy, tumor cells could be distinguished easily, which was contribute to the diagnosis of breast cancer. Moreover, the results were consistent with enzyme-linked immunosorbent assay that distinguished breast cancer patients by detecting the expression level of HER2 (Fig. S8B). These results demonstrated that DL-CHA was capable of sensing and imaging miRNA in cells from the whole blood samples, holding good potential in clinical application. Despite the good clinical applicability, this strategy cannot achieve the absolute quantification of intracellular miRNA, which should be further explored.

4. Conclusions

In summary, we have developed a simple sensing strategy for sensitive detection and imaging miRNAs in cells from whole blood based on DNA ladder formed by DL-CHA for the first time. Apart from having the unique features of accelerate response and improved sensitivity, DL-CHA exhibits several major merits as follows. Profiting from the novel notion that target induces the substrate transduction from dispersion into colocalization, DL-CHA possesses minimal leakage and greatly enhanced S/B ratio. Furthermore, the requirement of few kinds of DNA strands enables this strategy to simultaneously image multiple miRNAs by simply changing target-specific sequence. What's more, the practical application of DL-CHA has been demonstrated by sensing miRNA in cells from clinical blood samples. It is in principle possible to expand the

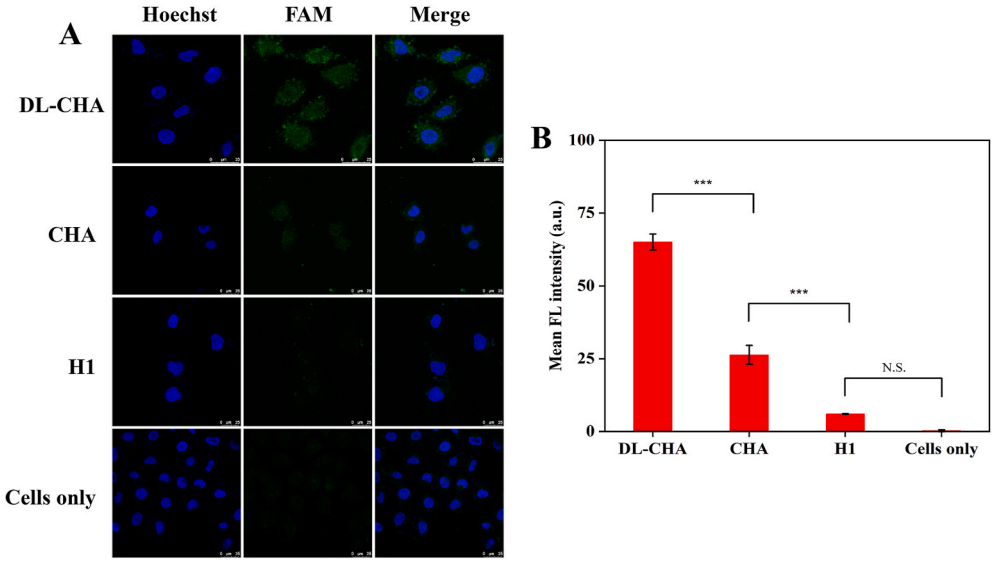

Fig. 4. (A) Confocal fluorescence images of untreated MCF-7 cells and MCF-7 cells incubated with DL-CHA, LH1, CHA, and H1, respectively. Scale bar is 25 μm. (B) The mean fluorescence intensity of the corresponding cells. The data error bars indicate mean ± SD (n = 3). ***$P < 0.001$. N.S., no significance.

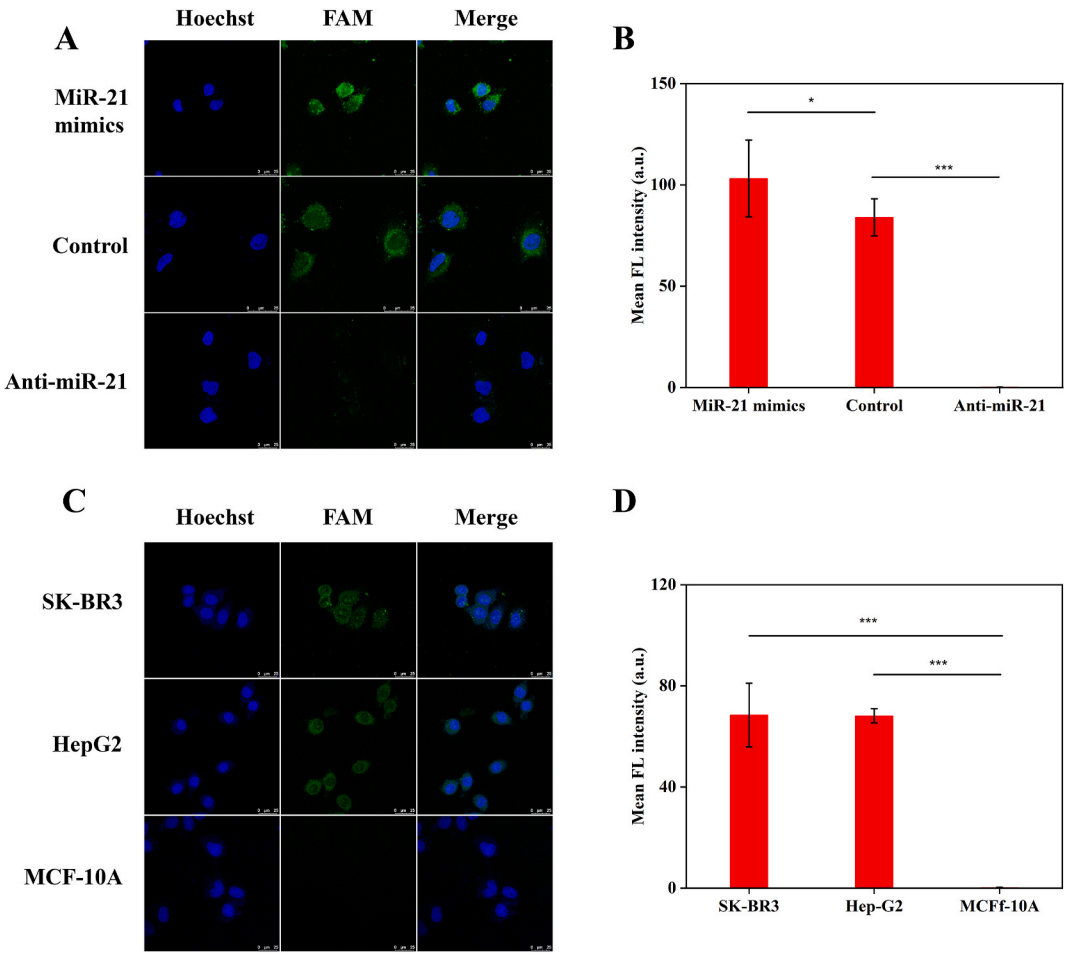

Fig. 5. (A) Confocal fluorescence images of MCF-7 cells treated with miR-21 mimics (top) or anti-miR-21 (bottom). (B) The mean fluorescence intensity of the cells with corresponding treatments. (C) Confocal fluorescence images of DL-CHA for detection of miR-21 in three kinds of cells (SK-BR3, HepG2, and MCF-10A cells). (D) The mean fluorescence intensity of corresponding cells. Scale bar is 25 μm. The data error bars indicate mean ± SD (n = 3). *P < 0.05, ***P < 0.001.

design concept into different nonenzymatic DNA circuits, such as HCR and EDC. Therefore, this work not only provides a powerful sensing tool for sensitive intracellular molecules detection, but opens up a much broader design space for the development of high-performance DNA circuits.

CRediT authorship contribution statement

Huijie Bai: Conceptualization, Methodology, Software, Investigation, Writing – original draft. **Yurong Yan:** Conceptualization, Methodology. **Dandan Li:** Software, Writing – original draft, Investigation. **Ningke Fan:** Methodology, Formal analysis, Software. **Wenqian Cheng:** Methodology, Formal analysis, Software. **Wei Yang:** Conceptualization, Data curation. **Huangxian Ju:** Conceptualization, Data curation. **Xinmin Li:** Writing – original draft, Software, Validation. **Shijia Ding:** Supervision, Data curation, Funding acquisition, Project administration.

Declaration of competing interest

We declare that we have no financial and personal relationships with other people or organizations that can inappropriately influence our work, there is no professional or other personal interest of any nature or kind in any product, service and/or company that could be construed as influencing the position presented in, or the review of, the manuscript entitled "**Dispersion-to-localization of catalytic hairpin assembly for sensitive sensing and imaging microRNAs in living cells from whole blood**".

Acknowledgements

This work was funded by the financial support from the Natural Science Foundation of China (81873980, 81702083), the National Science and Technology Major Project of the Ministry of Science and Technology of China (2018ZX10732202), and the Natural Science Foundation Project of Chongqing (cstc2018jcyjAX0349, cstc2020jcyj-msxm0190).

Appendix A. Supplementary data

Supplementary data to this article can be found online at https://doi.org/10.1016/j.bios.2021.113821.

References

Anfossi, S., Babayan, A., Pantel, K., Calin, G.A., 2018. Nat. Rev. Clin. Oncol. 15 (9), 541–563.
Chatterjee, G., Dalchau, N., Muscat, R.A., Phillips, A., Seelig, G., 2017. Nat. Nanotechnol. 12 (9), 920–927.
Cheglakov, Z., Cronin, T.M., He, C., Weizmann, Y., 2015. J. Am. Chem. Soc. 137 (19), 6116–6119.
Choi, C.K., Li, J., Wei, K., Xu, Y.J., Ho, L.W., Zhu, M., To, K.K., Choi, C.H., Bian, L., 2015. J. Am. Chem. Soc. 137 (23), 7337–7346.
Deng, R., Tang, L., Tian, Q., Wang, Y., Lin, L., Li, J., 2014. Angew Chem. Int. Ed. Engl. 53 (9), 2389–2393.
Deng, R., Zhang, K., Li, J., 2017. Acc. Chem. Res. 50 (4), 1059–1068.
Duan, L.Y., Liu, J.W., Yu, R.Q., Jiang, J.H., 2021. Biosens. Bioelectron. 177, 112976.

Gao, P., Liu, B., Pan, W., Li, N., Tang, B., 2020. Anal. Chem. 92 (12), 8459–8463.
Gebert, L.F.R., MacRae, I.J., 2019. Nat. Rev. Mol. Cell Biol. 20 (1), 21–37.
Goodall, G.J., Wickramasinghe, V.O., 2021. Nat. Rev. Cancer 21 (1), 22–36.
Huo, M., Li, S., Zhang, P., Feng, Y., Liu, Y., Wu, N., Ju, H., Ding, L., 2019. Anal. Chem. 91 (5), 3374–3381.
Karunanayake Mudiyanselage, A., Yu, Q., Leon-Duque, M.A., Zhao, B., Wu, R., You, M., 2018. J. Am. Chem. Soc. 140 (28), 8739–8745.
Li, B., Liu, Y., Liu, Y., Tian, T., Yang, B., Huang, X., Liu, J., Liu, B., 2020a. ACS Nano 14 (7), 8116–8125.
Li, J., Wang, A., Yang, X., Wang, K., Huang, J., 2021. Anal. Chem. 93 (15), 6270–6277.
Li, J., Wang, J., Liu, S., Xie, N., Quan, K., Yang, Y., Yang, X., Huang, J., Wang, K., 2020b. Angew Chem. Int. Ed. Engl. 59 (45), 20104–20111.
Liang, C.P., Ma, P.Q., Liu, H., Guo, X., Yin, B.C., Ye, B.C., 2017. Angew Chem. Int. Ed. Engl. 56 (31), 9077–9081.
Lin, F., Shao, Y., Wu, Y., Zhang, Y., 2021. ACS Appl. Mater. Interfaces 13 (3), 3713–3721.
Liu, H., Tian, T., Ji, D., Ren, N., Ge, S., Yan, M., Yu, J., 2016. Biosens. Bioelectron. 85, 909–914.
Liu, L., Rong, Q., Ke, G., Zhang, M., Li, J., Li, Y., Liu, Y., Chen, M., Zhang, X.B., 2019. Anal. Chem. 91 (5), 3675–3680.
Liu, P., Qian, X., Li, X., Fan, L., Li, X., Cui, D., Yan, Y., 2020a. ACS Appl. Mater. Interfaces 12 (40), 45648–45656.
Liu, R., Zhang, S., Zheng, T.T., Chen, Y.R., Wu, J.T., Wu, Z.S., 2020b. ACS Nano 14 (8), 9572–9584.
Mendell, J.T., Olson, E.N., 2012. Cell 148 (6), 1172–1187.
Meng, X., Wang, H., Yang, M., Li, J., Yang, F., Zhang, K., Dong, H., Zhang, X., 2021. Anal. Chem. 93 (3), 1693–1701.
Peng, H., Newbigging, A.M., Reid, M.S., Uppal, J.S., Xu, J., Zhang, H., Le, X.C., 2020. Anal. Chem. 92 (1), 292–308.
Qing, Z., Xu, J., Hu, J., Zheng, J., He, L., Zou, Z., Yang, S., Tan, W., Yang, R., 2019. Angew Chem. Int. Ed. Engl. 58 (34), 11574–11585.
Ren, K., Xu, Y., Liu, Y., Yang, M., Ju, H., 2018. ACS Nano 12 (1), 263–271.
Sun, X., Wei, B., Guo, Y., Xiao, S., Li, X., Yao, D., Yin, X., Liu, S., Liang, H., 2018. J. Am. Chem. Soc. 140 (31), 9979–9985.
Teichmann, M., Kopperger, E., Simmel, F.C., 2014. ACS Nano 8 (8), 8487–8496.
Tricoli, J.V., Jacobson, J.W., 2007. Cancer Res. 67 (10), 4553–4555.
Wei, J., Gong, X., Wang, Q., Pan, M., Liu, X., Liu, J., Xia, F., Wang, F., 2018a. Chem. Sci. 9 (1), 52–61.
Wei, J., Wang, H., Wu, Q., Gong, X., Ma, K., Liu, X., Wang, F., 2020. Angew Chem. Int. Ed. Engl. 59 (15), 5965–5971.
Wei, Q., Huang, J., Li, J., Wang, J., Yang, X., Liu, J., Wang, K., 2018b. Chem. Sci. 9 (40), 7802–7808.
Wu, Y., Meng, H.M., Chen, J., Jiang, K., Yang, R., Li, Y., Zhang, K., Qu, L., Zhang, X.B., Li, Z., 2020. Chem Commun (Camb). 56 (3), 470–473.
Xing, C., Chen, Z., Lin, Y., Wang, M., Xu, X., Dai, J., Wang, J., Lu, C., 2021. Chem Commun (Camb). 57 (26), 3251–3254.
Xue, C., Zhang, S.X., Ouyang, C.H., Chang, D., Salena, B.J., Li, Y., Wu, Z.S., 2018. Angew Chem. Int. Ed. Engl. 57 (31), 9739–9743.
Yang, F., Cheng, Y., Cao, Y., Zhang, Y., Dong, H., Lu, H., Zhang, X., 2019. Anal. Chem. 91 (15), 9828–9835.
Yang, Z., Zhang, S., Zhao, H., Niu, H., Wu, Z.S., Chang, H.T., 2018. Anal. Chem. 90 (23), 13891–13899.
Zhang, K., Meng, X., Yang, Z., Cao, Y., Cheng, Y., Wang, D., Lu, H., Shi, Z., Dong, H., Zhang, X., 2019. Adv Mater 31 (12), e1807888.
Zhu, D., Huang, J., Lu, B., Zhu, Y., Wei, Y., Zhang, Q., Guo, X., Yuwen, L., Su, S., Chao, J., Wang, L., 2019. ACS Appl. Mater. Interfaces 11 (23), 20725–20733.
Zhu, X., Qu, B., Ying, Z.M., Liu, J.W., Wu, Z., Yu, R.Q., Jiang, J.H., 2020. Anal. Chem. 92 (24), 15953–15958.